

# One-Dimensional van der Waals Material Tellurium: Raman Spectroscopy under Strain and Magneto-Transport

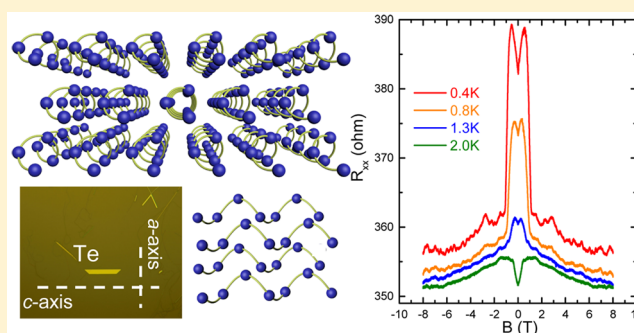
Yuchen Du,<sup>†,⊥</sup> Gang Qiu,<sup>†,⊥</sup> Yixiu Wang,<sup>‡</sup> Mengwei Si,<sup>†,⊥</sup> Xianfan Xu,<sup>§,⊥</sup> Wenzhuo Wu,<sup>\*,‡</sup> and Peide D. Ye<sup>\*,†,⊥</sup>

<sup>†</sup>School of Electrical and Computer Engineering, <sup>‡</sup>School of Industrial Engineering, <sup>§</sup>School of Mechanical Engineering, and <sup>⊥</sup>Birk Nanotechnology Center, Purdue University, West Lafayette, Indiana 47907, United States

**S** Supporting Information

**ABSTRACT:** Experimental demonstrations of one-dimensional (1D) van der Waals material tellurium (Te) have been presented by Raman spectroscopy under strain and magneto-transport. Raman spectroscopy measurements have been performed under strains along different principle axes. Pronounced strain response along the *c*-axis is observed due to the strong intrachain covalent bonds, while no strain response is obtained along the *a*-axis due to the weak interchain van der Waals interaction. Magneto-transport results further verify its anisotropic property, which results in dramatically distinct magneto-resistance behaviors in terms of three different magnetic field directions. Specifically, phase coherence length extracted from weak antilocalization effect,  $L_{\phi} \approx T^{-0.5}$ , claims its two-dimensional (2D) transport characteristics when an applied magnetic field is perpendicular to the thin film. In contrast,  $L_{\phi} \approx T^{-0.33}$  is obtained from universal conductance fluctuations once the magnetic field is along the *c*-axis of Te, which indicates its nature of 1D transport along the helical atomic chains. Our studies, which are obtained on high quality single crystal Te thin film, appear to serve as strong evidence of its 1D van der Waals structure from experimental perspectives. It is the aim of this paper to address this special concept that differs from the previous well-studied 1D nanowires or 2D van der Waals materials.

**KEYWORDS:** Tellurium, strain, Raman spectroscopy, magneto-transport, anisotropic, 1D van der Waals material



Chalcogens, more specifically, tellurium (Te) is a *p*-type semiconductor with a bandgap of  $\sim 0.35$  eV in bulk and  $\sim 1$  eV in monolayer.<sup>1–7</sup> The importance of introducing Te is not only based on the fact that it is an elemental metallic bonding-based piezoelectric material,<sup>8–10</sup> but also that it has an asymmetric crystal structure in its radial direction. The trigonal crystalline form of Te is an array of parallel atomic chains arranged on a 2D hexagonal lattice. The packing of the chains is determined by the dashed lines in Figure 1a, which are pure van der Waals forces in the basal plane. The solid lines designate the primary covalent bonds in the chain.<sup>11,12</sup> As is evident in Figure 1a, Te has a highly anisotropic crystal structure, and it consists of helical chains along the *c*-axis that are bound with other chains by van der Waals interactions. Because of its special crystal structure, the synthesis of Te is divided into two primary categories. The single 1D Te nanowire has been achieved by a variety of synthesis methods such as microwave-assisted synthesis in ionic liquid,<sup>13</sup> vapor phase growth,<sup>14</sup> and solution phase synthesis,<sup>15–17</sup> where the growth mechanism involves the nucleation of spherical particles followed by the growth of 1D nanostructure along the *c*-axis, and the diameter of the nanowires ranges from a few to hundreds of nanometers. Two-dimensional (2D) hexagonal Te nanoplates can also be realized via high-temperature vapor phase process,<sup>18</sup> in which

the developed Te nanoplates share the same crystal geometry as its basal unit cell, and the thickness and lateral dimension of 2D Te hexagonal nanoplate are up to several hundred nanometers. 2D Te crystals packed along *a*-axis with van der Waals forces, as shown in Figure 1b, with Te atomic chains along primary *c*-axis, have not been realized.

Recently, we have demonstrated a substrate-free solution phase process to synthesize a new type of large-area, high-quality 2D single crystal Te films, which exhibit process-dependent thickness ranging from a few to tens of nanometers.<sup>19</sup> The as-fabricated Te field-effect transistors demonstrate large on/off ratio ( $\sim 10^6$ ), high field-effect mobilities ( $\sim 700$  cm<sup>2</sup>/(V s)), and excessive drain current of  $\sim 600$  mA/mm at 100 nm channel length,<sup>19</sup> which are comparable or superior to transistors made of other experimentally accessible 2D semiconductors. In great contrast to black phosphorus and other environmentally sensitive 2D crystals, 2D Te thin film has a pronounced air-stability. The significance of this work stands on the fact that the synthesized Te thin films have revealed mostly in trapezoid shape, where the length and width of the

**Received:** April 23, 2017  
**Revised:** May 30, 2017  
**Published:** May 31, 2017

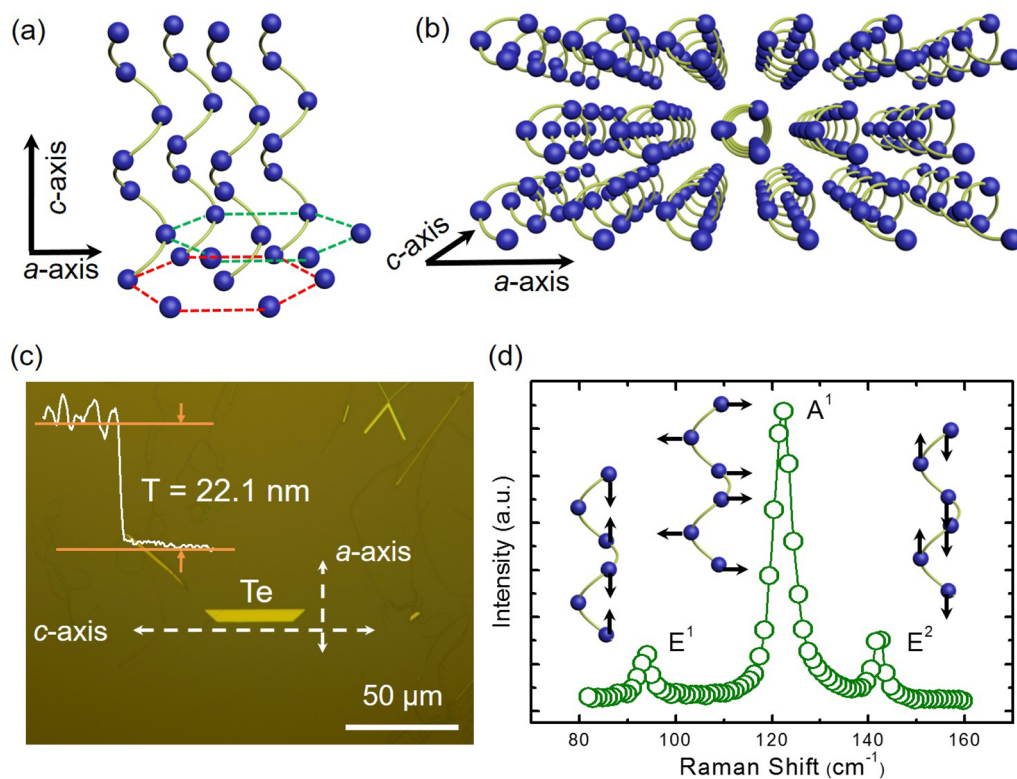


**Figure 1.** Te characterization. (a, b) Lattice structure of Te. Packing of the chains is determined by the green and red dashed lines, which represent pure van der Waals force in the basal plane. Solid yellow lines designate the primary covalent bonds. Each Te atom shares covalent bonds with its two nearest neighbors in the chain. Every fourth atom is directly located above another atom so that the projection of the chain on a plane perpendicular to the chain direction is an equilateral triangle. (c) Optical image of the 22.1 nm thick Te thin film with two principle lattice orientations. Scale bar in optical image is 50  $\mu\text{m}$ . (d) Atomic vibrational patterns of  $E^1$ ,  $A^1$ , and  $E^2$  phonon modes in Te Raman spectra and their corresponding atom vibration directions.

films can be up to  $\sim 100 \mu\text{m}$  and  $\sim 10 \mu\text{m}$ , respectively. The liquid phase synthesized Te films have a distinct crystal structure as illustrated in Figure 1b and c, which differs from 1D Te nanowires or 2D van der Waals hexagonal Te thin film. Raman spectroscopy and transport measurements confirm that the as-synthesized Te films have all covalent 1D atomic chains along primary  $c$ -axis as long as 100  $\mu\text{m}$ , while all helical chains are stacked together by van der Waals force along  $a$ -axis as wide as 10  $\mu\text{m}$ .

In this Letter, we have employed Raman spectroscopy to experimentally verify the 1D van der Waals structure of the Te thin films with respect to strains along different principle axes. The significant strain response along the  $c$ -axis, together with no response along the  $a$ -axis, has clearly demonstrated its 1D van der Waals nature and the anisotropic atomic structure. Red-shifted/blue-shifted Raman spectra of Te along  $c$ -axis under tensile/compressive strain can be interpreted as the result of deformation of covalent bond length in 1D helical chains, and the absence of Raman shift along strained  $a$ -axis reveals its weak van der Waals interaction between atomic chains. We have also carried out magneto-transport studies of Te thin films with magnetic fields along three principle axes. The measurement results further verify its anisotropic property with dramatically different characteristics. Temperature dependent phase coherence length extracted from weak antilocalization effect (WAL),  $L_\phi \approx T^{-0.5}$ , claims its 2D transport behavior when an applied magnetic field is perpendicular to  $x$ - $y$  plane. The WAL effect is vanished with the applied magnetic field in the 2D film plane but perpendicular to the Te helical atomic chains, and Hall

resistance is independent of the magnetic fields, which indicates an out-of-plane Hall effect. Furthermore,  $L_\phi \approx T^{-0.33}$  is obtained from universal conductance fluctuations (UCF) once an applied magnetic field is along the  $c$ -axis of Te, indicating its nature of 1D transport mechanism. Our studies, which are obtained on high-quality single crystal Te thin films, serve as strong experimental evidence of its 1D van der Waals structure. The work presented in this Letter adds a new class of 2D crystals, made of 1D van der Waals materials, to the well-studied 2D materials family or quasi-1D materials.<sup>20,21</sup>

**Crystal Structure and Lattice Vibration of Te.** Te crystallizes in a hexagonal structure, and every fourth atom is directly located above another atom in its chain so that the projection of the chain on a plane perpendicular to the chain direction is an equilateral triangle. The hexagonal lattice is achieved by locating a chain at the center and at each of the six corners of a hexagon. Te atoms are covalently connected via an infinite helical turn at  $120^\circ$  along its longitudinal [0001] direction, which is defined as  $c$ -axis. All turns are bounded to hexagonal bundles in its radial direction by weak van der Waals force that has been defined as  $a$ -axis,<sup>11,12</sup> which is the in-plane direction of the 2D Te in this experiment.<sup>19</sup> To start our experiment, Te thin film was synthesized and transferred to a conducting Si substrate with a 300 nm  $\text{SiO}_2$  capping layer.<sup>19</sup> A typical optical image of Te thin film is given in Figure 1c, with a thickness of 22.1 nm determined by atomic force microscopy (AFM). Identified Te thin films have this trapezoid shape, which make it easy to classify  $c$ -axis versus  $a$ -axis. Raman spectroscopy in Figure 1d shows Te thin film has three active

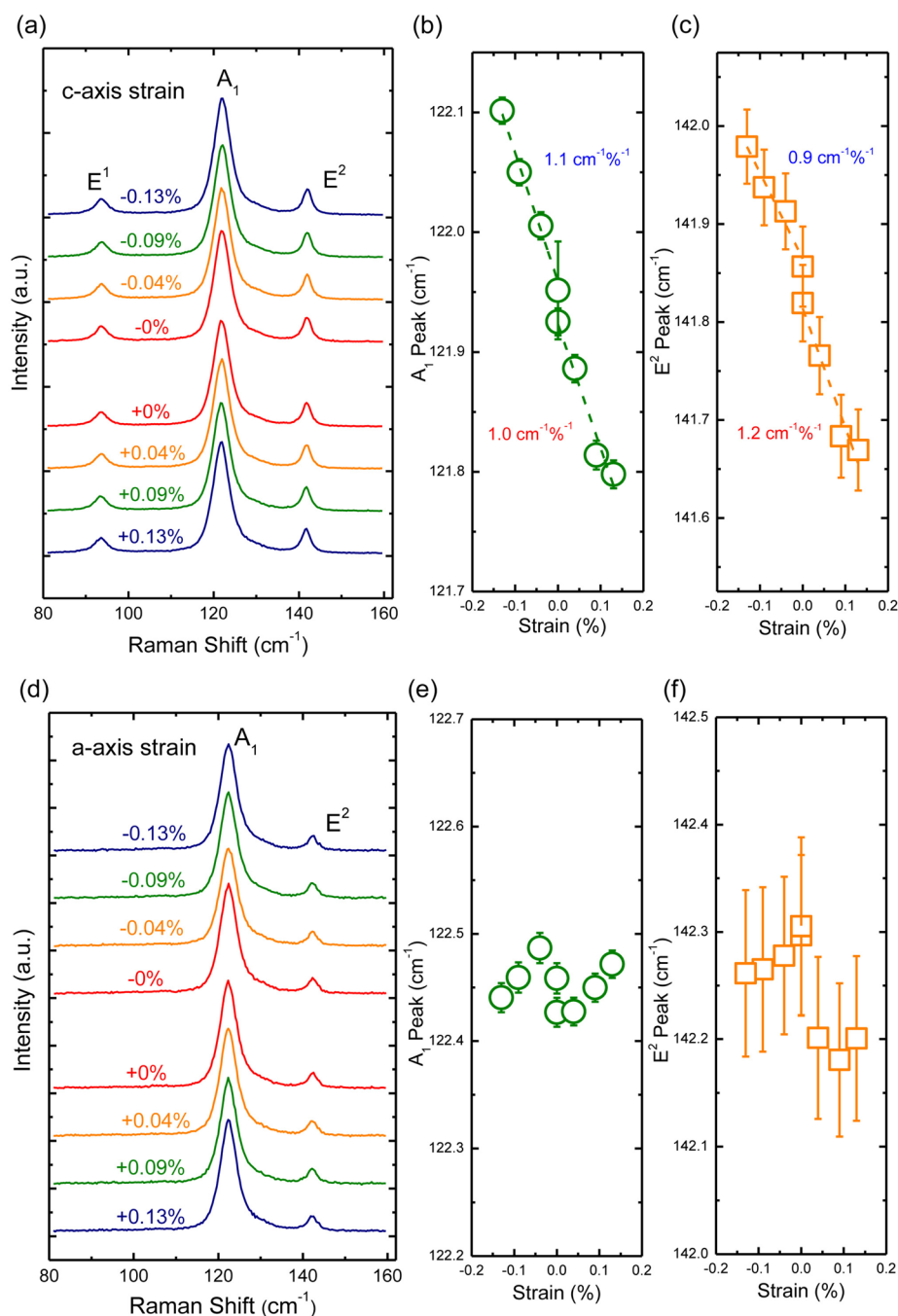


**Figure 2.** Raman evolution of uniaxial strained Te. (a) Raman spectra of Te thin film for both tensile and compressive  $c$ -axis strains. Raman shift of (b)  $A_1$  and (c)  $E^2$  modes in  $c$ -axis strained Te. (d) Raman spectra of Te thin film for both tensile and compressive  $a$ -axis strains. Raman shift of (e)  $A_1$  and (f)  $E^2$  modes in  $a$ -axis strained Te. The dashed lines show linear fit results, and error bars are determined from Lorentzian peak fittings.

Raman phonon modes. The most intense Raman peak of Te located at  $\sim 122 \text{ cm}^{-1}$  is related to the  $A_1$  mode, corresponding to chain expansion mode in which each atom moves in the basal plane.<sup>12</sup> Meanwhile, there exist two degenerate E modes, which separate into predominately bond-bending and bond-stretching types with larger admixture in Te.<sup>12</sup>  $E^1$  mode at  $\sim 94 \text{ cm}^{-1}$  is caused by  $a$ -axis rotation, and  $E^2$  mode at  $142 \text{ cm}^{-1}$  is appointed to asymmetric stretching mainly along the  $c$ -axis.<sup>12</sup>

#### Significant Strain-Response along 1D Covalent $c$ -Axis.

We first investigated the evolution of the Raman spectra of Te with uniaxial tensile and compressive strains, summarized in Figure 2a. The laser polarization is aligned along the  $a$ -axis of

Te thin film, and the strain direction is along  $c$ -axis based on our apparatus setup.<sup>22</sup> In our work, we used Lorentzian function to fit the Raman spectra and obtained the peak frequency of each mode at different strain strengths. For unstrained Te, consistent with previous reports,<sup>3,18,23,24</sup> we observe the  $A_1$  mode at  $\sim 122 \text{ cm}^{-1}$  and modes of  $E^1$  and  $E^2$  at  $\sim 94 \text{ cm}^{-1}$  and  $\sim 142 \text{ cm}^{-1}$ , respectively. The  $A_1$  and  $E^2$  modes show the same linear trend of Raman frequency shift with respect to the applied strains, while the rates of frequency shift are different in these two modes. Both  $A_1$  and  $E^2$  modes experience a blue-shift when Te is under compressive strains along the  $c$ -axis, with a slope of  $1.1 \text{ cm}^{-1}\%^{-1}$  and  $0.9 \text{ cm}^{-1}\%^{-1}$ ,

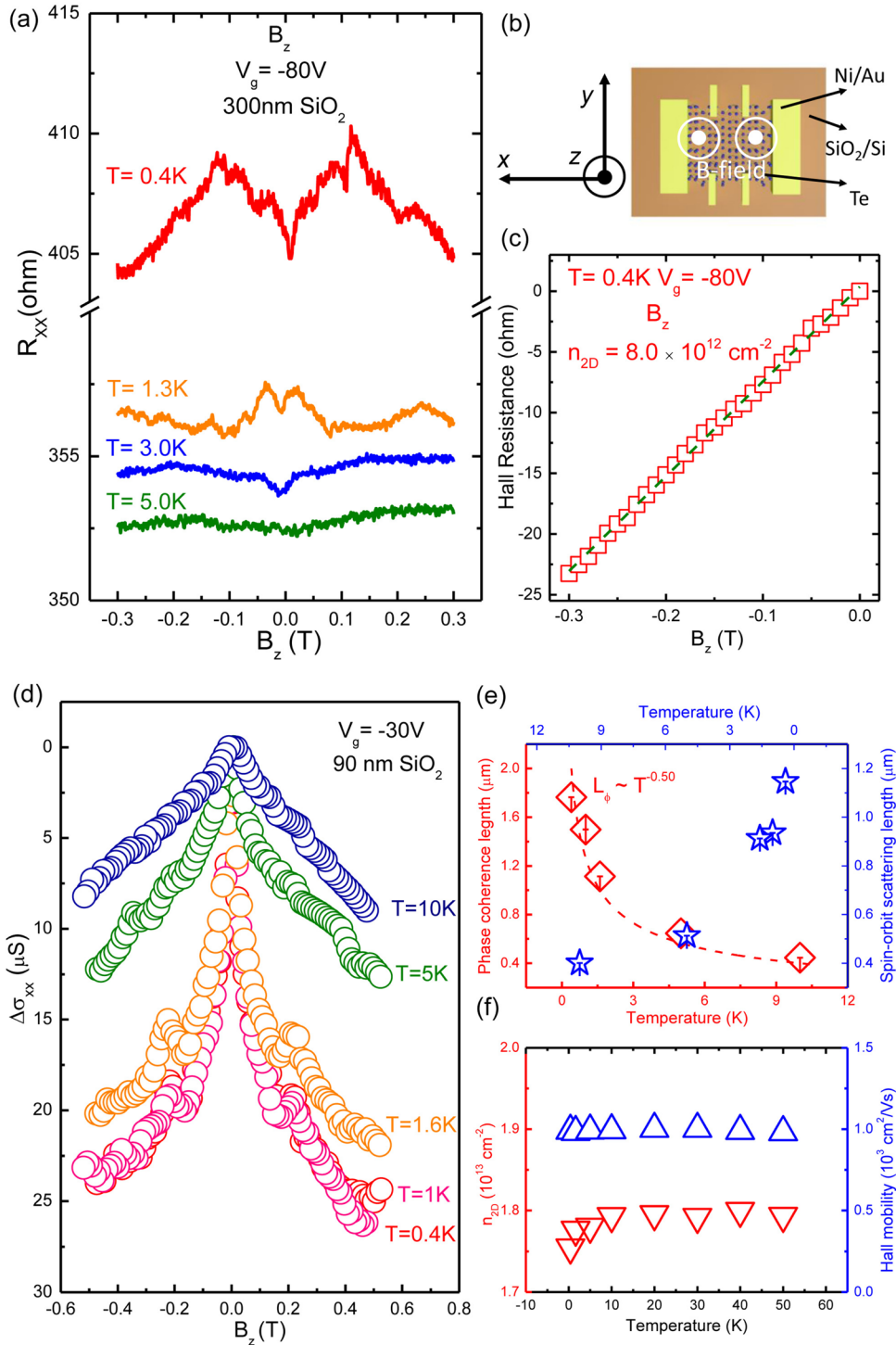


**Figure 3.** Magneto-transport of Te in  $B_z$  direction. (a) Magneto-resistance of Te thin film with varied  $B_z$  field for different temperatures. The sample has a back-gate bias of  $-80$  V, where the  $\text{SiO}_2$  thickness is  $300$  nm. (b) Device scheme configuration and magnetic field indicator. (c) Hall effect of Te thin film with varied  $B_z$  field at base temperature of  $0.4$  K, and  $-80$  V. (d) A different sample that has a pronounced WAL effect. The WAL effect has been measured from  $0.4$  K, up to  $10$  K. The back-gate bias is  $-30$  V, in which the back-gate dielectric is  $90$  nm instead. (e) Phase coherence length and spin-orbit scattering length extracted from WAL effect vary with measured temperatures. The phase coherence length has demonstrated a strong power-law behavior, and dashed line indicates theoretical simulation  $L_\phi \approx T^\gamma$  with a power exponent  $\gamma = 0.50$ . Our experimental results match the theoretical prediction that carrier scattering would give  $L_\phi$  proportional to  $T^{-0.5}$  in the 2D system. Error bars are determined from HNL fittings. (f) 2D carrier density and Hall mobility as a function of temperatures.

respectively. On the other hand,  $A_1$  and  $E^2$  have a red-shift at a rate of  $1.0 \text{ cm}^{-1}\%$  and  $1.2 \text{ cm}^{-1}\%$  under uniaxial tensile strains along the  $c$ -axis, as shown in Figure 2b and c. Note that we did not observe a measurable Raman shift in the  $E^1$  mode,

where the  $E^1$  peak position remains the same with various  $c$ -axis strains and we ascribe it to the fact  $E^1$  mode is responsible to  $a$ -axis rotation and is not sensitive to  $c$ -axis deformation.<sup>12,23,24</sup> The different responses of Raman spectra with strains can be

explained by analyzing the types of vibration mode involved. Let us take the  $E^2$  mode as an example in the first place, where the atomic motions of  $E^2$  mode occur along the 1D  $c$ -axis direction. The red-shift of the  $E^2$  mode under tensile strain along the  $c$ -axis, with a slope of  $1.2 \text{ cm}^{-1}\%^{-1}$ , can be understood based on the elongation of the Te–Te covalent bond length, which weakens the interatomic interactions and therefore reduces the vibration frequency.<sup>22,25</sup> Meanwhile, blue-shift with a slope of  $0.9 \text{ cm}^{-1}\%^{-1}$  under compressive strain indicates the enhancement of interatomic interaction, thus interpreted as a result of the shortened covalent Te–Te bond under compressive deformation. Furthermore, tensile strain not only enlarges the Te–Te bond length assigned to  $E^2$  mode along  $c$ -axis, but also influences the basal plane displacement pattern, which is associated with  $A_1$  mode. The red-shifted/blue-shifted Raman frequency of the  $A_1$  mode is attributed to the decreased/increased equilateral triangle projection of the chain on basal plane perpendicular to the  $c$ -axis, thus manipulating the basal plane vibration frequency and leading to Raman shift of  $A_1$  mode.

**Zero Strain-Response along van der Waals  $a$ -Axis.** To apply strain along the  $a$ -axis, the Te sample substrate was rotated by  $90^\circ$ , and the Raman spectroscopy was introduced along the  $c$ -axis on the same sample. The corresponding Raman spectra of  $a$ -axis strained Te are presented in Figure 2d, where the  $E^1$  mode has disappeared due to the optical anisotropic property reported previously that  $E^1$  mode maximizes when Raman polarization is along  $a$ -axis, and vanishes when it is along  $c$ -axis.<sup>19</sup> Figure 2e and f illustrate the  $A_1$  and  $E^2$  peak positions as a function of tensile and compressive  $a$ -axis strains. Interestingly, both  $A_1$  and  $E^2$  have no response with various tensile and compressive strains, and the  $A_1$  and  $E^2$  Raman peak positions are independent of applied strains. The response along  $a$ -axis strain is totally different from that along  $c$ -axis, providing strong evidence of its anisotropic behavior. More importantly, the significant strain response along  $c$ -axis, together with no response along  $a$ -axis has conclusively verified the 1D van der Waals nature of Te thin film. The pronounced strain response when the deformation is applied along  $c$ -axis is directly associated with interatomic interactions between 1D covalent Te–Te bonds, while the absence of strain response in  $a$ -axis strains demonstrates no covalent bond, but pure weak van der Waals interaction in 2D plane of Te thin films.

**Magneto-Transport Property of Te in  $B_z$  Direction.** Several sources of literature have previously studied the anisotropic electrical behaviors of bulk Te, showing that resistivities of intrinsic Te at room temperature are  $\rho_{\parallel} = 0.26 \text{ } \Omega \text{ cm}$  and  $\rho_{\perp} = 0.51 \text{ } \Omega \text{ cm}$ , parallel and perpendicular to the  $c$ -axis, respectively.<sup>11</sup> However, the anisotropic magneto-transport properties of synthesized 1D van der Waals Te thin film have never been reported. The anisotropic magneto-transport properties with their temperature dependence are presented below. In the first experiment, the applied magnetic field is in  $z$ -direction and perpendicular to the  $x$ – $y$  thin film plane. In the second experiment, the magnetic field is in  $y$ -direction along the  $a$ -axis of Te thin film. In the third experiment, the magnetic field is aligned to 1D Te atomic chains,  $c$ -axis, which is defined as the  $x$ -direction (Figure 3b).

We first present the magneto-transport results of Te in  $B_z$  direction, in which the magnetic field is applied perpendicularly to the 2D thin film plane. Magneto-resistance ( $R_{xx}$ ) measurements of a typical Te thin film at different temperatures from 0.4–5.0 K are presented in Figure 3a.  $R_{xx}$  exhibits a

characteristic dip at small magnetic field regime, and this phenomenon is identified as WAL, indicating an existence of strong spin–orbit interaction in Te originated from its high atomic number and large electronic polarizability.<sup>26</sup> The WAL effect comes from a system with spin–orbit coupling in which the spin of a carrier is coupled to its orbit momentum.<sup>27</sup> The spin of the carrier rotates as it goes around a self-intersecting path, and the direction of this rotation is opposite for the two branches of the loop. Because of this, the two paths along any loop interfere destructively, which leads to a lower net resistivity.<sup>28–32</sup> The importance of WAL is based on the consequence of spin-momentum locking and the full suppression of backscattering, resulting in a relative  $\pi$  Berry phase acquired by carriers executing time-reversed paths. WAL is not an effect possessed only by Dirac materials, such as topological insulators and graphene, but a generic characteristic of the materials with strong spin–orbit coupling. WAL is temperature dependent as shown in Figure 3a. We measured more than 10 devices with different film thickness, charge density, and mobility. All show WAL characteristic. We use another sample with a similar thickness of 27.0 nm but more pronounced WAL features for the quantitative analysis presented here (Figure 3d). As expected, the effect is strongly temperature-dependent and shows a deep peak at base temperature of 0.4 K. In addition, the effect diminishes when the temperature increases to 10 K, at which the localization is suppressed due to the decreased phase coherence length and spin–orbit scattering length at higher temperatures. We consider Hikami–Larkin–Nagaoka (HLN)<sup>32</sup> formula in the presence of spin–orbit coupling to discuss the WAL effect in  $B_z$  field. We fit the low-field portion of the magneto-conductance curves using the HLN model:

$$\Delta\sigma(B) = \sigma(B) - \sigma(B = 0) = n_s n_v \left( F\left(\frac{B}{B_\phi + B_{so}}\right) - \frac{1}{n_s} \left( F\left(\frac{B}{B_\phi}\right) - F\left(\frac{B}{B_\phi + 2B_{so}}\right) \right) \right) \quad (1)$$

$$F(Z) = \psi\left(\frac{1}{2} + \frac{1}{Z}\right) + \ln(Z), \quad B_\phi = \frac{\hbar}{4eL_\phi}, \quad B_{so} = \frac{\hbar}{4eL_{so}} \quad (2)$$

where  $\psi$  is the digamma function,  $L_\phi$  is the phase coherence length,  $L_{so}$  is the spin–orbit scattering length,  $e$  is the electronic charge,  $\hbar$  is Planck's constant,  $B$  is the magnetic field, and  $n_s$  and  $n_v$  are spin degeneracy and valley degeneracy, respectively. Figure 3e shows the phase coherence length  $L_\phi$  and the spin–orbit scattering length  $L_{so}$  as a function of temperature. We should note that the maximum phase coherence length extracted from the small magnetic field portion is  $\sim 1.8 \text{ } \mu\text{m}$  at 0.4 K at  $-30 \text{ V}$  back gate bias. As we increase the temperature from 0.4 to 10 K, the temperature dependence of the phase coherence length demonstrates a strong power-law behavior of  $L_\phi \approx T^{-\gamma}$  with a power exponent  $\gamma$  approximately 0.5. This value matches the observation from previous studies that electron–electron or hole–hole scattering would give  $L_\phi$  proportional to  $T^{-0.5}$  in a 2D system.<sup>33</sup> However, more refined experiments are needed to reveal its special transport property of 1D van der Waals structure in 2D thin film system when the

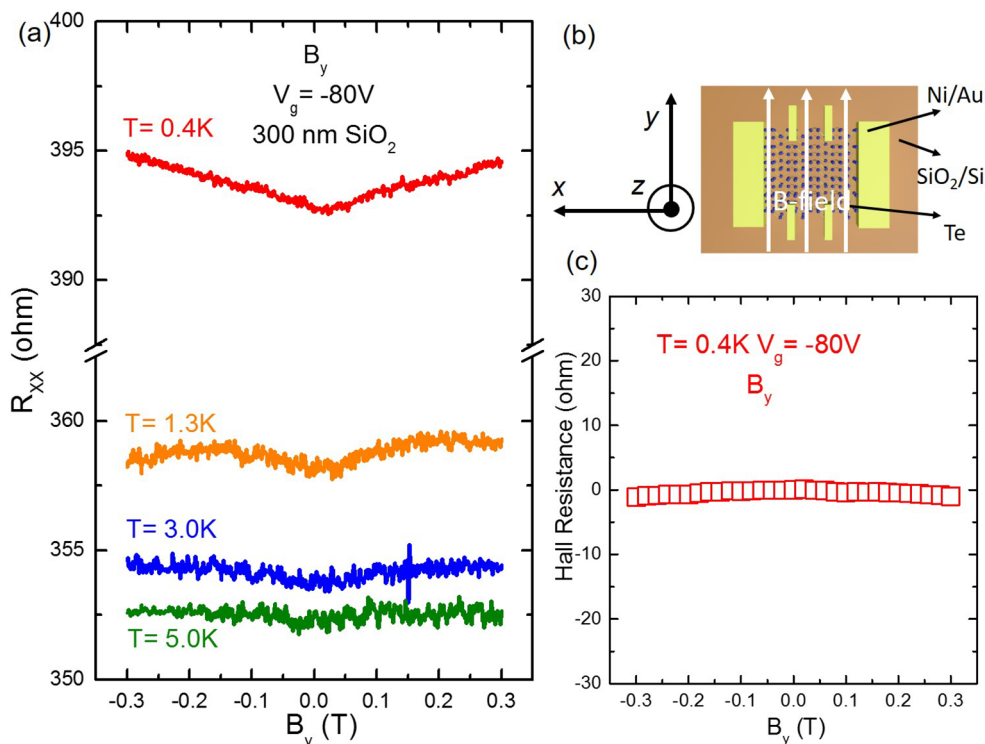


**Figure 4.** Magneto-transport of Te in  $B_y$  direction. (a) Magneto-resistance of Te thin film with varied  $B_y$  field for different temperatures. The sample has a back-gate bias of  $-80\text{ V}$ , where the  $\text{SiO}_2$  thickness is  $300\text{ nm}$ . (b) Device scheme configuration and magnetic field indicator. (c) Hall effect of Te thin film with varied  $B_y$  field at base temperature of  $0.4\text{ K}$ , and  $-80\text{ V}$ .

magnetic field is perpendicular to the 2D plane. We find that  $L_{\text{so}}$  is also temperature dependent, and the maximum spin-orbit scattering length at base temperature of  $0.4\text{ K}$  is  $\sim 1.1\ \mu\text{m}$ , and this number is promising for future Te-based spintronics applications. Temperature dependences of carrier concentration and mobility of Te are examined in this work as well, as depicted in Figure 3f. The 2D carrier density  $n_{2\text{D}}$  is determined from  $n_{2\text{D}} = \frac{B}{e\rho_{xy}}$ , with a magnitude of  $1.8 \times 10^{13}\text{ cm}^{-2}$  in thin film

Te is recorded at  $-30\text{ V}$  back gate bias and  $0.4\text{ K}$ . Hall mobility, obtained from  $\mu_{\text{H}} = \frac{L}{W} \frac{1}{R_{xx}n_{2\text{D}}e}$ , where  $L$  is the channel length,  $W$  is the channel width, and  $R_{xx}$  is the longitudinal resistance, has been measured with various temperatures. The Hall mobility remains constant at cryogenic temperatures with a maximum value of  $\sim 1002\text{ cm}^2/(\text{V s})$ . We calculate the mean free path of Te thin films by applying equation:

$$l_{\text{m}} = \tau v_{\text{F}} \quad (3)$$

where  $\tau$  is mean free time, and  $v_{\text{F}}$  is Fermi velocity. Related mobility and 2D carrier density are extracted from Figure 3e and f. The estimated mean free path is  $\sim 700\text{ nm}$  at  $\mu = 1002\text{ cm}^2/(\text{V s})$  and  $n_{2\text{D}} = 1.8 \times 10^{13}\text{ cm}^{-2}$ , which is comparable with our coherence length extracted from WAL effect. In our experiment, more than 10 samples have been systematically fabricated and measured, and a maximum mean free path of  $\sim 1\ \mu\text{m}$  is obtained with a sample that has  $\mu \sim 2000\text{ cm}^2/(\text{V s})$  and  $n_{2\text{D}} \approx 8 \times 10^{12}\text{ cm}^{-2}$ , which indicates a decent quality of our single crystal Te thin films.

#### Magneto-Transport Property of Te in $B_y$ Direction.

The  $R_{xx}$  of the same sample with the magnetic field in  $B_y$  direction is presented in Figure 4. The WAL effect is vanished with the applied  $B_y$  magnetic field in the 2D film plane but

perpendicular to the Te helical atomic chains. As shown in Figure 4, we do not observe any pronounced characteristics in magneto-resistance and Hall resistance depending on the applied external magnetic field in this configuration.

#### Magneto-Transport Property of Te in $B_x$ Direction.

The last and the most important experiment is the magneto-transport properties of Te thin film in  $B_x$  direction, where the applied magnetic field is in line with 1D  $c$ -axis. Figure 5a shows the magneto-resistance of Te at different temperatures, in which the WAL effect is also observed within small magnetic field regime. In addition, UCF effect has been observed in our Te thin film at high fields. UCF is a quantum interference effect of diffusive charge carriers, observed commonly in the mesoscopic systems of semiconductors, metals, and 2D Dirac graphene. The mesoscopic nature or finite size of a weakly disordered sample results in the loss of the self-averaging of its physical properties.<sup>34,35</sup> Applying a magnetic field in semiconductors varies the phase of the wave function of a charge carrier, where the magnitude and interval of conductance fluctuation are closely related to the phase coherence length. The UCF effect, as presented in Figure 5c, is observed in our Te thin film sample within the moderate magnetic field and low temperature regime, and this phenomenon is robust and persists to increased temperature up to  $2\text{ K}$ . The periodic conductance fluctuation patterns can be observed repeatedly, and they present the similar features in the different magneto-conductance curves measured at different temperatures. To quantitatively compare the measured UCF magnitudes with theoretical predictions, we have generated root-mean-square (rms) magnitude of the magneto-conductivity fluctuations:

$$\Delta G_{\text{rms}} = \sqrt{\langle [\Delta G(B) - \langle \Delta G(B) \rangle]^2 \rangle} \quad (4)$$

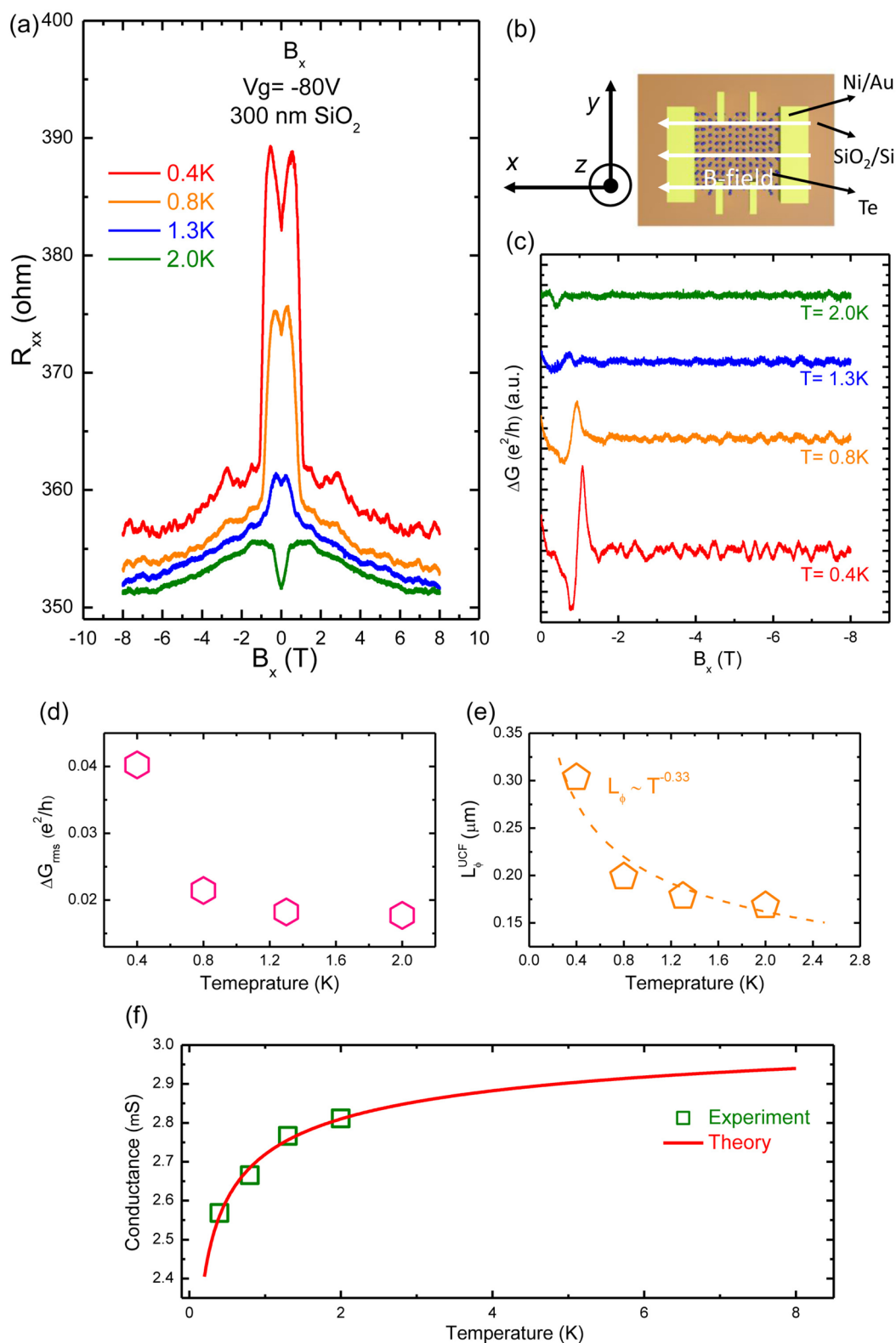


**Figure 5.** Magneto-transport of Te in  $B_x$  direction. (a) Magneto-resistance of Te thin film with varied  $B_x$  field for different temperatures. The sample has a back-gate bias of  $-80$  V, where the  $\text{SiO}_2$  thickness is  $300$  nm. (b) Device scheme configuration and magnetic field indicator. (c)  $\Delta G(T)$  curves with varied  $B_x$  field. The UCF effect is robust and persists to increased temperature up to  $2$  K. (d)  $\Delta G_{\text{rms}}$  changes with different measured temperatures. (e) Phase coherence length has demonstrated a strong power-law behavior, and dashed line indicates theoretical simulation  $L_{\phi} \approx T^{-\gamma}$  with a power exponent  $\gamma = 0.33$ . Our experimental results match the theoretical prediction that carrier scattering would give  $L_{\phi}$  proportional to  $T^{-0.33}$  in the 1D system. (f) Temperature dependence of the conductance at zero magnetic field. The red solid line is theoretical prediction, and green squares are experimental data.

where  $\langle \dots \rangle$  denotes an average over the magnetic field, which is an ensemble average over impurity configurations. Extracted  $\Delta G_{\text{rms}}$  is demonstrated in Figure 5d with different temperatures. UCF theory predicts a fluctuation magnitude of  $0.73 e^2/h$  for a weakly disordered, 1D mesoscopic wire at  $T = 0$  K and at zero magnetic field.<sup>33</sup> At  $T > 0$  K, we limit our discussion to the 1D regime where the coherence length is much shorter than the sample size  $L$  ( $6 \mu\text{m}$ ), and the Te chain can be considered as a series of uncorrelated segments of length  $L_{\phi}^{\text{UCF}}$ . The relation between fluctuations rms and  $L_{\phi}^{\text{UCF}}$  can be described in 1D system as<sup>35–37</sup>

$$\Delta G_{\text{rms}} = \sqrt{12} \frac{e^2}{h} \left( \frac{L_{\phi}^{\text{UCF}}}{L} \right)^{3/2} \quad (5)$$

The obtained values of  $L_{\phi}^{\text{UCF}}$  extracted from observed UCF amplitudes can be used to verify the anisotropic property by comparing with  $L_{\phi}$  from WAL effect along  $B_z$ . As shown in Figure 5e, the behavior of  $L_{\phi}^{\text{UCF}}$  is significantly different from what we saw in Figure 3e, and we interpret it as the result of the anisotropic transport in Te where 1D chain transport differs from 2D thin film transport. The extracted phase coherence lengths from UCF follow a power law dependence of temperature  $L_{\phi} \approx T^{-0.33}$ , consistent with the dephasing mechanism being the carrier–carrier collisions with small energy transfers as observed commonly in 1D nanowire systems with an exponent value of 0.33.<sup>36,37</sup> Finally, we discuss the pronounced temperature-dependent features of the conductance near zero magnetic field, presented in Figure 5a as huge peaks in magneto-resistance. Because of the localization effect within the small magnetic fields, it is hard to determine the real conductance at exact zero magnetic field. Instead of reading the numbers at magnetic field equals to zero, we use peak conductance near  $\pm 0.5T$  as  $\sigma(B = 0)$  which we believe this value is approximately the intrinsic zero-field magneto-conductance with localization effect excluded. For the maximum gate bias of  $-80$  V, conductance  $\sigma$  in 1D system is given by<sup>28</sup>

$$\sigma(T) = \sigma_0 - \frac{2e^2}{h} \frac{L_{\phi}}{L} \quad (6)$$

Since we have found that  $L_{\phi} \approx T^{-0.33}$ , we can rearrange our equation by replacing with phase coherence length with temperature. We fitted our experimental data from  $0.4$  K up to  $2.0$  K with a constant Drude conductance, and theoretical prediction is shown in red solid line as depicted in Figure 5f. The functional form of the fit is consistent with the experimental data within low temperature since our discussions are in quantum coherent regime. This result further confirms the 1D transport nature of Te thin films when the applied magnetic field is aligned with the helical atomic chains.

In summary, we have experimentally demonstrated the 1D van der Waals structure of Te thin film synthesized recently by our liquid phase method. Mechanical strain experiments have been conducted to verify its anisotropic crystal structure, in which the strong intrachain covalent bond gives rise to the significant strain response along  $c$ -axis, and the zero strain-response along  $a$ -axis is due to the van der Waals interaction between helical chains. In addition, magneto-transport of Te with three different magnetic configurations proves its anisotropic property, which results in dramatically distinct magneto-resistance behaviors. Specifically, phase coherence

length extracted from WAL effect,  $L_{\phi} \approx T^{-0.5}$  claims its 2D transport behavior when  $B$ -field is perpendicular to  $x$ – $y$  plane. More experiment needs to be conducted to further verify its 2D carrier transport upon 1D structure. In contrast,  $L_{\phi} \approx T^{-0.33}$  is obtained from UCF when the magnetic field is along  $c$ -axis of Te, which confirms its nature of 1D transport mechanism. The power exponent of a value of  $-0.33$  validates the special lattice structure of Te, where the magneto-transport is along the helical chain.

**Sample Synthesis.** The samples were grown through the reduction of sodium tellurite ( $\text{Na}_2\text{TeO}_3$ ) by hydrazine hydrate ( $\text{N}_2\text{H}_4$ ) in an alkaline solution at temperatures from  $160$ – $200$  °C with the presence of crystal-face-blocking ligand polyvinylpyrrolidone (PVP). The amount of hydrazine is maintained at a high level to ensure the complete reduction of  $\text{TeO}_3^{2-}$  into Te. A controlled, slow release of the Te source was achieved under the alkaline condition for maintaining the Te concentration, critical for the kinetic control of the 2D growth. The Te thin films were then transferred onto a  $\text{SiO}_2/\text{Si}$  substrate after a postsynthesis Langmuir–Blodgett assembly process and used for fabrication process.

**Raman Measurements.** All Raman measurements were carried out on a HORIBA LabRAM HR800 Raman spectrometer. The system is equipped with a He–Ne excitation laser (wavelength  $632.8$  nm), an  $1800$  g/mm grating, and a Nikon  $50\times$  ( $\text{NA} = 0.45$ ) long-working-distance objective lens. Subsequent Raman spectroscopy of strained Te studies was performed under an excitation laser power of  $0.17$  mW, sufficiently low to avoid excessive sample heating.

**Te Thin Film Device Fabrication.** Thin film Te with a similar thickness as compared to strain experiment was transferred from solution to a heavily doped silicon substrate with a  $\text{SiO}_2$  capping layer. Hall bars were defined by the e-beam lithography, followed by Ni/Au contacts, deposited via e-beam evaporation. A magnitude of  $100$  nA input current was sent from the source to the drain, which is large enough to minimize measurement noise, but not too much to induce current heating at low temperature. Transport measurements were carried out in a  $\text{He}^3$  cryostat with a superconducting magnet using a Stanford Research 830 lock-in amplifier.

## ■ ASSOCIATED CONTENT

### 📄 Supporting Information

The Supporting Information is available free of charge on the ACS Publications website at DOI: [10.1021/acs.nanolett.7b01717](https://doi.org/10.1021/acs.nanolett.7b01717).

Additional details for repeatability of strain experiment, air-stability of Raman spectra, laser polarization configurations, magneto-resistance of  $B_z$  direction in large  $B$  field, Hall effect measurements of  $B_z$  direction, gate-dependent measurements of  $B_x$  direction (PDF)

## ■ AUTHOR INFORMATION

### Corresponding Authors

\*E-mail: [yep@purdue.edu](mailto:yep@purdue.edu).

\*E-mail: [wenzhuowu@purdue.edu](mailto:wenzhuowu@purdue.edu).

### ORCID

Peide D. Ye: [0000-0001-8466-9745](https://orcid.org/0000-0001-8466-9745)

### Author Contributions

P.D.Y. and W.W. conceived the idea and designed and supervised the experiments. Y.D. performed the strain experiments and analyzed the experimental data. Y.D., G.Q., and M.S.

performed magneto-transport experiments and analyzed the experimental data. Y.W. synthesized Te thin films. X.X. supported Raman spectra measurements. Y.D., G.Q., Y.W., M.S., X.X., W.W., and P.D.Y. cowrote the manuscript.

#### Notes

The authors declare no competing financial interest.

#### ACKNOWLEDGMENTS

The authors would like to thank Prof. Leonid Rokhinson and Zhong Wan for valuable discussions and experiment support. The authors would also like to thank Tim Murphy, Ju-Hyun Park, Glover Jones, and Hongwoo Baek at National High Magnetic Field Laboratory for the technical assistance.

#### REFERENCES

- (1) Von Hippel, A. *J. Chem. Phys.* **1948**, *16*, 372–380.
- (2) Cherin, P. T.; Unger, P. *Acta Crystallogr.* **1967**, *23*, 670–671.
- (3) Hoerstel, W.; Kusnick, D.; Spitzer, M. *Phys. Status Solidi B* **1973**, *60*, 213–221.
- (4) Doi, T.; Nakao, K.; Kamimura, H. *J. Phys. Soc. Jpn.* **1970**, *28*, 36–43.
- (5) Coker, A.; Lee, T.; Das, T. P. *Phys. Rev. B: Condens. Matter Mater. Phys.* **1980**, *22*, 2968.
- (6) Zhu, Z.; Cai, C.; Wang, C.; Sun, Q.; Han, X.; Guo, Z.; Jia, Y. *arXiv:1605.03253*, **2016**.
- (7) Zhu, Z.; Cai, X.; Niu, C.; Yi, S.; Guo, Z.; Liu, F.; Cho, J.-H.; Jia, Y.; Zhang, Z. *arXiv:1701.08875*, **2017**.
- (8) Liu, J. W.; Zhu, J. H.; Zhang, C. L.; Liang, H. W.; Yu, S. H. *J. Am. Chem. Soc.* **2010**, *132*, 8945–8952.
- (9) Lin, S.; Li, W.; Chen, Z.; Shen, J.; Ge, B.; Pei, Y. *Nat. Commun.* **2016**, *7*, 10287.
- (10) Lee, T. I.; Lee, S.; Lee, E.; Sohn, S.; Lee, Y.; Lee, S.; Moon, G.; Kim, D.; Kim, Y. S.; Myoung, J. M.; Wang, Z. L. *Adv. Mater.* **2013**, *25*, 2920–2925.
- (11) Epstein, A. S.; Fritzsche, H.; Lark-Horovitz, K. *Phys. Rev.* **1957**, *107*, 412.
- (12) Martin, R. M.; Lucovsky, G.; Helliwell, K. *Phys. Rev. B* **1976**, *13*, 1383.
- (13) Zhu, Y. J.; Wang, W. W.; Qi, R. J.; Hu, X. L. *Angew. Chem.* **2004**, *116*, 1434–1438.
- (14) Hawley, C. J.; Beatty, B. R.; Chen, G.; Spanier, J. E. *Cryst. Growth Des.* **2012**, *12*, 2789–2793.
- (15) Mo, M.; Zeng, J.; Liu, X.; Yu, W.; Zhang, S.; Qian, Y. *Adv. Mater.* **2002**, *14*, 1658–1662.
- (16) Mayers, B.; Xia, Y. *J. Mater. Chem.* **2002**, *12*, 1875–1881.
- (17) Gates, B.; Yin, Y.; Xia, Y. *J. Am. Chem. Soc.* **2000**, *122*, 12582–12583.
- (18) Wang, Q.; Safdar, M.; Xu, K.; Mirza, M.; Wang, Z.; He, J. *ACS Nano* **2014**, *8*, 7497–7505.
- (19) Wang, Y.; Qiu, G.; Wang, Q.; Liu, Y.; Du, Y.; Wang, R.; Goddard, W. A.; Kim, M. J.; Ye, P. D.; Wu, W. *arXiv:1704.06202*, **2017**.
- (20) Stolyarov, M. A.; Liu, G.; Bloodgood, M. A.; Aytan, E.; Jiang, C.; Samnakay, R.; Salguero, T. T.; Nika, D. L.; Romyantsev, S. L.; Shur, M. S.; Bozhilov, K. N.; Balandin, A. A. *Nanoscale* **2016**, *8*, 15774–15782.
- (21) Liu, G.; Romyantsev, S.; Bloodgood, M. A.; Salguero, T. T.; Shur, M. S.; Balandin, A. A. *Nano Lett.* **2017**, *17*, 377–383.
- (22) Du, Y.; Maassen, J.; Wu, W.; Luo, Z.; Xu, X.; Ye, P. D. *Nano Lett.* **2016**, *16*, 6701–6708.
- (23) Pine, A. S.; Dresselhaus, G. *Phys. Rev. B* **1971**, *4*, 356.
- (24) Torrie, B. H. *Solid State Commun.* **1970**, *8*, 1899–1901.
- (25) Harrison, W. A. *Elementary Electronic Structure*; World Scientific: Singapore, 1999.
- (26) Xian, L.; Paz, A. P.; Bianco, E.; Ajayan, P. M.; Rubio, A. *arXiv:1607.01555*, **2016**.
- (27) Hirayama, M.; Okugawa, R.; Ishibashi, S.; Murakami, S.; Miyake, T. *Phys. Rev. Lett.* **2015**, *114*, 206401.
- (28) Datta, S. *Electronic Transport in Mesoscopic System*; Cambridge University Press, 1997.
- (29) Naito, M.; Tanaka, S. *J. Phys. Soc. Jpn.* **1982**, *51*, 219–227.
- (30) Fukuyama, H. *Suppl. Prog. Theor. Phys.* **1980**, *69*, 220–231.
- (31) Fukuyama, H. *J. Phys. Soc. Jpn.* **1980**, *49*, 649–651.
- (32) Hikami, S.; Larkin, A. I.; Nagaoka, Y. *Prog. Theor. Phys.* **1980**, *63*, 707–710.
- (33) Altshuler, B. L.; Aronov, A. G. *Electron–Electron Interaction in Disordered Systems*; Elsevier: North-Holland, 1985.
- (34) Lee, P. A.; Stone, A. D.; Fukuyama, H. *Phys. Rev. B: Condens. Matter Mater. Phys.* **1987**, *35*, 1039.
- (35) Beenakker, C. W. J.; van Houten, H. *Solid State Phys.* **1991**, *44*, 1–228.
- (36) Yang, P.-Y.; Wang, L. Y.; Hsu, Y.-W.; Lin, J.-J. *Phys. Rev. B: Condens. Matter Mater. Phys.* **2012**, *85*, 085423.
- (37) Liang, D.; Sakr, M. R.; Gao, X. P. A. *Nano Lett.* **2009**, *9*, 1709–1712.